Article

Single-Mode Input Fiber Combined with Multimode Sensing Fiber Used in Brillouin Optical Time-Domain Reflectometry

Yongqian Li [1,2,3], Haijun Fan [1,2,3,*], Lixin Zhang [1,2,3], Zijuan Liu [1,2,3], Lei Wang [1,2,3], Jiaqi Wu [1,2,3] and Shaokang Wang [1,2,3]

[1] Department of Electronic and Communication Engineering, North China Electric Power University, Baoding 071003, China; liyq@ncepu.edu.cn (Y.L.); lxzhang@ncepu.edu.cn (L.Z.); lzijuan@ncepu.edu.cn (Z.L.); hdbdwl@ncepu.edu.cn (L.W.); wujiaqi@ncepu.edu.cn (J.W.); wsk@ncepu.edu.cn (S.W.)

[2] Hebei Key Laboratory of Power Internet of Things Technology, North China Electric Power University, Baoding 071003, China

[3] Baoding Key Laboratory of Optical Fiber Sensing and Optical Communication Technology, North China Electric Power University, Baoding 071003, China

* Correspondence: fhj@ncepu.edu.cn

Abstract: Conventional single-mode fiber (SMF) Brillouin optical time-domain reflectometry (BOTDR) suffers from a low signal-to-noise ratio (SNR) and severe sensing reliability due to the influence of the stimulated Brillouin scattering threshold and bend loss. In this study, a simple and low-cost distributed sensing structure, with a single-mode input fiber alignment fusion and a 50 μm diameter graded index multimode sensing fiber, is designed, and the SNR characteristic is investigated. Through theoretical derivation and experimental verification, a higher SNR and excellent bending resistance are realized in BOTDR. The experimentally measured improvements in the SNR of the proposed sensing structure over the SMF at the beginning and end of a 5 km fiber are 2.5 dB and 1.3 dB, respectively. The minimum bending radius of the sensing structure is 2.25 mm, which is much better than that of the SMFs. The bidirectional optical losses between the SMF and the 50 μm graded index multimode fiber are measured by a simple experiment system and are 0.106 dB and 1.35 dB, respectively. The temperature-sensing characteristics of the sensing structure are measured by the self-built frequency-shift local heterodyne BOTDR sensor, and the measured temperature sensitivity and accuracy are 0.946 MHz/°C and 1 °C, respectively. The design provides a reference for BOTDR with a high SNR and has great potential for structural safety and health monitoring of infrastructures.

Keywords: Brillouin optical time domain reflectometry; multimode fiber; bidirectional optical coupling efficiency; signal-to-noise ratio; bending resistance

1. Introduction

Brillouin distributed optical fiber sensors using a light wave as a carrier, fiber as a medium, and scattering as a mechanism can realize distributed temperature and strain sensing with a high measurement accuracy and have been extensively studied for use sensing applications for structural safety and health monitoring (SSHM) in recent years [1–11]. In previous research on Brillouin sensing, the most commonly used sensing fibers were standard single-mode fibers (SMFs) [2–8]. However, in recent years, with the diversification of human needs and the improvement of technological means, some special fibers have started to enter the public view, such as polymer optical fibers [9,12], large effective area fibers [13], few-mode fibers [14,15], high-delta optical fibers [16], photonic crystal fibers [17], and multicore fibers [18,19]. These special fibers make up for the shortcomings of the SMF more or less, but their complex structures and expensive prices make them unable to shake the cornerstone position of SMF in the field of optical fiber sensing. However, the input power and signal-to-noise ratio (SNR) of SMF Brillouin sensing are small due to the limitations of the single-ended stimulated Brillouin scattering (SBS) effect,

which further affects the measurement accuracy and sensing distance [5]. Moreover, in practical engineering applications, the poor bending resistance of SMF makes it difficult to overcome the bend loss caused by the harsh construction environment, causing the loss or even interruption of the Brillouin scattering signal. To solve this problem, G.657 B3 fibers have been designed. At 1550 nm, the loss of G.657 B3 is 0.15 dB/turn with a bending radius of 5 mm [20]. Although a significant improvement over G.652, it is still difficult to satisfy the requirements of applications in complex engineering environments. Since then, a number of bend-resistant special fibers have emerged, such as trench-assisted fibers [21–23], hole-assisted fibers [24–26], and photonic crystal fibers [27–29]. The goal is to introduce a trench refractive index profile around the fiber core to suppress the optical signal loss caused by bends. Moreover, some fiber producers, such as Draka, Corning, and OFS, are also developing bend-resistant fibers, among which the F-SBC fiber from OFS is particularly impressive, with a maximum bend loss of only 0.0005 dB/turn and a bending radius of 5 mm at 1550 nm. However, the complex structures of these special fibers make the preparation process cumbersome and expensive, and they are not the best choice for SSHM in terms of cost effectiveness for kilometre-scale infrastructure. Therefore, it is necessary to explore a low-cost, high-SNR, and bend-resistant fiber to make up for the SMF deficiency in extremely complex engineering environments.

In this manuscript, we fuse a short SMF with a 50 μm diameter graded index multimode fiber (GI-MMF) and combine it with self-built frequency-shifted local heterodyne Brillouin optical time-domain reflectometry (BOTDR) to form a low-cost, high-SNR, and bend-resistant distributed sensor. In our sensing structure, the SMF is used to excite the fundamental mode in the 50 μm GI-MMF and to filter out the high-order modes in the scattering signal, which is conducive to improving the measurement accuracy. Although the fusion of the two fibers is not a new structure and is mostly used in micronano sensors [30,31], its Brillouin scattering properties and applications in distributed fiber sensing have not been reported on by anyone other than us [32]. Moreover, most previous studies on Brillouin sensing in MMFs have focused on the entire MMF sensing structure and the SBS threshold (SBST) characteristics, in which mode coupling severely affects the Brillouin gain spectrum (BGS) and sensing performance [33–36]. We first design and construct a simple system to evaluate the bidirectional optical coupling efficiency of the SMF and 50 μm GI-MMF. Moreover, we theoretically and experimentally investigate the high-SNR characteristic of the proposed sensing structure. By suppressing the Fresnel reflection signal from the far end of the sensing structure, we also prove that the sensing structure has a good bending resistance, with a minimum bending radius of 2.25 mm. Finally, a BOTDR system is designed and built to measure and evaluate the temperature-sensing characteristics of the designed sensing structure, proving its sensing reliability.

2. Theory

2.1. BGS of MMF

As an early fiber, MMF has played an important role in medium-range and medium-capacity optical fiber communication systems in recent years. MMF can transmit many modes with different electromagnetic field distributions, characteristic parameters, and Brillouin scattering spectra. When the pump light is injected into the MMF, the Stokes light is generated by the interactions between the photons and acoustic phonons. The Stokes light suffers a Doppler shift called a Brillouin frequency shift (BFS), which can be written as follows [37]:

$$v_{\mathrm{B}} = \frac{2 n_{mn} V_{\mathrm{A}}}{\lambda} \sin(\phi_{mn}/2). \tag{1}$$

where λ is the optical wavelength; n_{mn} and ϕ_{mn} are the refractive index and scattering angle, respectively; m denotes the number of whole standing waves distributed along the circumference of the field; n denotes the number of half standing waves distributed along the radial direction of the field, $\phi_{mn} \in [2\arccos(\mathrm{NA}/n_1), \pi]$ [37]; and V_{A} is the acoustic velocity in MMF.

The BGS model of MMF can be described by [38]

$$g(v) = g_0 \frac{\Delta v_{BS}/2}{v_{B0} - v_{Bc}} \times \left[\tan^{-1}\left(\frac{v_{B0} - v}{\Delta v_{BS}/2}\right) - \tan^{-1}\left(\frac{v_{Bc} - v}{\Delta v_{BS}/2}\right) \right], \tag{2}$$

$$v_{B0} = v_B(\phi)|_{\phi=\pi} = \frac{2n_0 V_A}{\lambda}, \tag{3}$$

$$v_{Bc} = v_B(\phi)|_{\phi=\pi-2\theta_c} = \frac{2n_0 V_A}{\lambda} \sin\left(\frac{\pi - 2\theta_c}{2}\right)$$

$$= \frac{2n_0 V_A \sqrt{1 - (NA)^2/n_0^2}}{\lambda}. \tag{4}$$

where g_0 is the Brillouin gain coefficient of SMF, v is the frequency shift value, v_{B0} and v_{Bc} are the on-axis (maximum) and critical angle (minimum) BFS, respectively. Δv_{BS} is the BGS linewidth of SMF, ϕ is the backward Stokes angle, θ_c is the complementary angle of the critical angle, NA is the numerical aperture, and n_0 is the refractive index of the MMF core. The Brillouin gain spectra of MMF and SMF are illustrated in Figure 1. It can be seen that the BFS of the MMF is smaller than that of the SMF, which is caused by the different light incident angles and scattering directions. Moreover, multiple Brillouin-gain spectra exist in the MMF, resulting in a relatively wider BGS and a smaller Brillouin-gain coefficient (2.096×10^{-11} m/W).
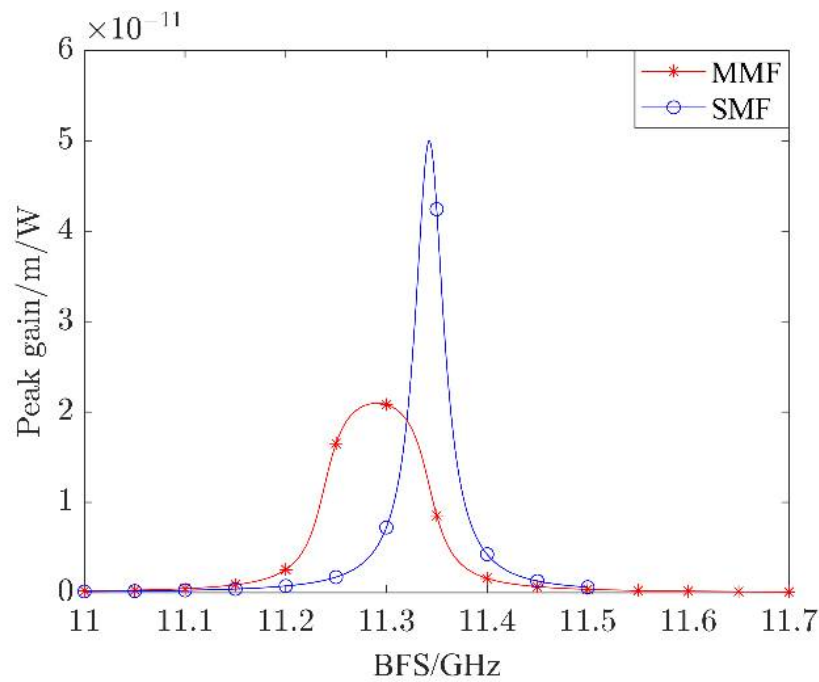

Figure 1. Brillouin gain spectra of MMF and SMF.

2.2. Improvement of SNR

In fiber Brillouin sensing, the injection intensity of light is limited by the SBST. When the injection intensity exceeds the SBST, most of the energy of the pump light is rapidly transferred to the Stokes light, severely limiting the sensing quality and distance. The SBSTs of the fibers can be expressed as [35]

$$P_{th} = G A_{eff} / g_i L_{eff}, \tag{5}$$

$$G \approx \ln\left[\frac{4 A_{eff} v_B B^{3/2} \pi^{1/2} \lambda}{g_i L_{eff} k T \tau c}\right]. \tag{6}$$

where g_i denotes the Brillouin gain coefficient of SMF ($i = 0$) or MMF ($i = 1$), L_{eff}; and α and A_{eff} are the effective length, attenuation coefficient, and the effective area, respectively. G is the threshold coefficient, $\tau = 1/T_B$ is the phonon attenuation rate, T_B is the phonon lifetime, c is the light velocity in vacuum, v_B is the BFS, T is the thermodynamic temperature, and $B = 21$, k is the Boltzmann constant. From Equations (5) and (6), it can be seen that the SBST of the fiber is mainly related to the effective area and the Brillouin-gain coefficient. Compared to the SMF, the MMF has a smaller Brillouin gain and a larger effective area, providing it with a higher SBST. Therefore, when using MMF as sensing fiber, it is expected that a higher SNR will be obtained. The improvement in the SNR (ISNR) can be expressed as [21,39]

$$I_{SNR}(z) = P_M(z)e^{-\alpha_M z}/P_S(z)e^{-\alpha_S z}, \tag{7}$$

where α_M and α_S are the attenuation coefficients of MMF and SMF, respectively, and $P_M(z)$ and $P_S(z)$ are the BGS peak powers at position z of MMF and SMF, respectively.

$$P(z) = P_0 \alpha_B ScWe^{-\alpha z}/(2n_{eff}), \tag{8}$$

where W is the pulse width, P_0 is the peak power, n_{eff} is the effective refractive index, and α_B is the Brillouin scattering coefficient. S is the backscattering coefficient, which can be written as follows [40]:

$$S = (\lambda/n_{eff})^2/4\pi A_{eff}, \tag{9}$$

$$\alpha_B = 8\pi^3 n_{eff}{}^8 p_{12}^2 kT/\left(3\rho\lambda^4 V_A^2\right). \tag{10}$$

where p_{12} is the photoelastic coefficient, and ρ is the density.

It can be seen from the analysis that the SBSTs of MMF and SMF are obviously different at the same length, which makes the maximum launched pulse-peak power also different for the two fibers. The maximum allowable pulse peak power of the fiber is

$$P_{0th} = P_{th}\frac{L_{eff}}{L_p} = P_{th}\frac{2nL_{eff}}{cW}. \tag{11}$$

where L_p is the effective length of the pulse. For the 50 μm GI-MMF and SMF, the maximum pulse peak power ratio is

$$\frac{P_{0thM}}{P_{0thS}} = \frac{P_{thM}L_{effM}/L_p}{P_{thS}L_{effS}/L_p} = \frac{g_0 G_M A_{effM}}{g_1 G_S A_{effS}} \approx \frac{g_0 A_{effM}}{g_1 A_{effS}} \approx 5. \tag{12}$$

$$A_{effM} = \pi\omega^2 = \pi\left[\left(\sqrt{\frac{2}{V}} + \frac{0.23}{V^{3/2}} + \frac{18.01}{V^6}\right)a\right]^2, \tag{13}$$

where P_{thM} and P_{thS}, P_{0thM} and P_{0thS}, L_{effM} and L_{effS}, A_{effM} and A_{effS}, and G_M and G_S are the SBST, maximum pulse-peak power, effective length, effective area, and the threshold coefficient of the 50 μm GI-MMF and SMF, respectively. ω and a are the mode field radius and the core radius of MMF, respectively, and V is the normalized frequency. From Equations (6) and (12), it can be seen that the pulse peak power of the 50 μm GI-MMF is approximately five times higher than that of the SMF. Furthermore, although the attenuation coefficient, fiber length, pump wavelength, and ambient temperature also affect the maximum pulse-peak power ratio between GI-MMF and SMF, the main influencing factor is the difference in the Brillouin gain and effective area caused by the different fiber structures.

Substituting Equations (5), (6) and (8)–(11) into Equation (7) and keeping the launched fiber pulse power as the maximum allowable value, the ISNR expression is

$$
\begin{aligned}
I_{\mathrm{SNR}}(z) \quad &= P_{\mathrm{M}}(z)e^{-\alpha_{\mathrm{M}}z} / P_{\mathrm{S}}(z)e^{-\alpha_{\mathrm{S}}z} \\
&= \frac{P_{0\mathrm{thM}}\alpha_{BM}S_{\mathrm{M}}cWe^{-2\alpha_{\mathrm{M}}z}/2n_{\mathrm{effM}}}{P_{0\mathrm{thS}}\alpha_{BS}S_{\mathrm{S}}cWe^{-2\alpha_{\mathrm{S}}z}/2n_{\mathrm{effS}}} \\
&= \frac{2n_{\mathrm{effS}}P_{0\mathrm{thM}}\alpha_{BM}S_{\mathrm{M}}cWe^{-2\alpha_{\mathrm{M}}z}}{2n_{\mathrm{effM}}P_{0\mathrm{thS}}\alpha_{BS}S_{\mathrm{S}}cWe^{-2\alpha_{\mathrm{S}}z}} \\
&= \frac{n_{\mathrm{effS}}}{n_{\mathrm{effM}}}\frac{g_0 G_{\mathrm{M}}A_{\mathrm{effM}}}{g_1 G_{\mathrm{S}}A_{\mathrm{effS}}}\frac{n_{\mathrm{effM}}^8}{n_{\mathrm{effS}}^8}\frac{n_{\mathrm{effS}}^2 A_{\mathrm{effS}}e^{-2\alpha_{\mathrm{M}}z}}{n_{\mathrm{effM}}^2 A_{\mathrm{effM}}e^{-2\alpha_{\mathrm{S}}z}} \\
&= \frac{g_0}{g_1}\frac{n_{\mathrm{effM}}^5}{n_{\mathrm{effS}}^5}\frac{G_{\mathrm{M}}}{G_{\mathrm{S}}}\frac{e^{-2\alpha_{\mathrm{M}}z}}{e^{-2\alpha_{\mathrm{S}}z}} \approx 2.39\frac{e^{-2\alpha_{\mathrm{M}}z}}{e^{-2\alpha_{\mathrm{S}}z}}.
\end{aligned} \tag{14}
$$

where n_{effM} and n_{effS}, and S_{M} and S_{S} are the effective refractive index and backscattering coefficient of the 50 μm GI-MMF and SMF, respectively. Equation (14) shows that the SNR of the 50 μm GI-MMF is more than twice that of the SMF and that it has the same length and attenuation under the conditions of the maximum allowable pulse power input. Moreover, the attenuation coefficient of these two types of fibers is also a major factor affecting the ISNR.

When the ISNR > 0 dB, it means that the SNR of the proposed sensing structure is higher than that of the SMF. In order to make the results more intuitive, we combined Equation (14) with the basic parameters of the two types of optical fibers in Table 1, and the results are shown in Figure 2. It can be seen from Figure 2 that the 50 μm GI-MMF can accommodate a higher optical power for a higher SNR due to its higher SBST and pulse-peak power. We performed calculations on the fibers that were utilized in the experiment and obtained the ISNR of the 50 μm GI-MMF over that of the SMF. The results, which are displayed in Figure 2a, were 3.558 dB at the beginning and 1.452 dB at the end. It should be pointed out that the ISNRs at the beginning and the end are not identical; this is mostly the results of the two fibers having distinct attenuation coefficients. The ISNR has a particularly steep slope as a result of the relatively large magnitude of the MMF's attenuation coefficient. In fact, as fiber production technology has improved, the attenuation coefficient of the MMF has been reduced considerably. As a result, as shown in Figure 2b, another 50 μm GI-MMF with a lower attenuation coefficient was determined. It can be seen that the ISNR is more than 0 dB in a specific range, indicating that the suggested sensing structure has a higher SNR than SMF.
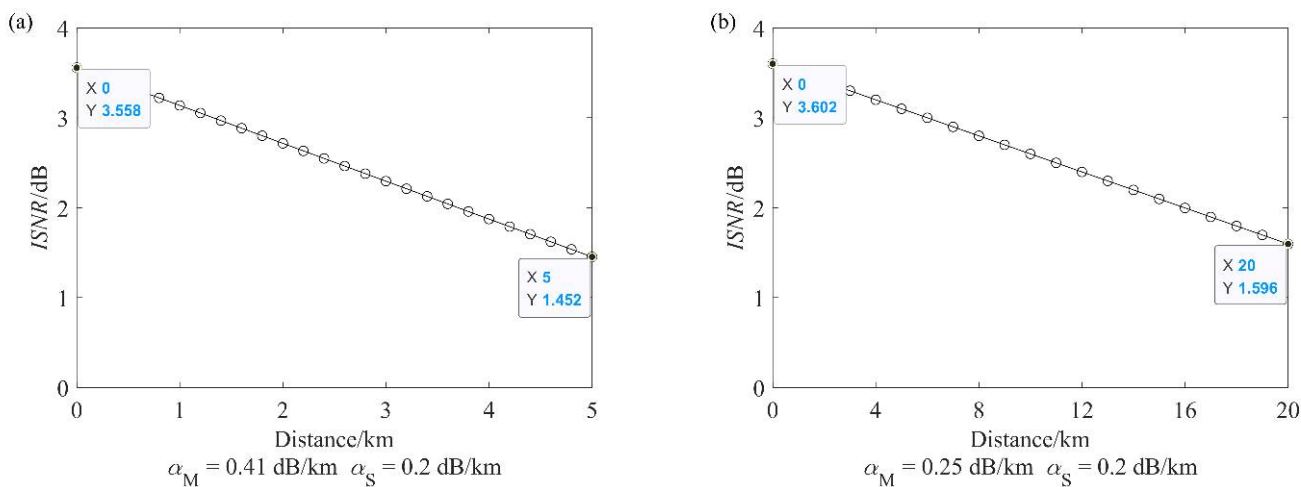

Figure 2. The calculated ISNR of the designed sensing structure over SMF in the BOTDR system. (**a**) 5 km; (**b**) 20 km.

Table 1. Simulation parameters of two sensing structures.

Parameter (Units)	g_0 (m/W)	g_1 (m/W)	B	T_B (ns)
Value	5×10^{-11}	2.096×10^{-11}	21	10
Parameter (Units)	V_A (m/s)	k (J/K)	T (K)	λ (nm)
Value	5940	1.38×10^{-23}	300	1550
Parameter (Units)	v_B (GHz)	A_{effS} (m^2)	n_{effS}	p_{12}
Value	11	9.5×10^{-11}	1.45	0.27
Parameter (Units)	ρ (kg/m^3)	A_{effM} (m^2)	n_{effM}	W (ns)
Value	2200	1.9677×10^{-10}	1.48	130

2.3. Fundamental Mode Excitation and High-Order Modes Filtering in GI-MMF

The number of modes that can be transmitted in the MMF is given by [41]:

$$M = \left(\frac{g}{g+2} \right) \frac{V^2}{2} \tag{15}$$

$$V = k_0 a N A \tag{16}$$

$$k_0 = \frac{2\pi}{\lambda} \tag{17}$$

where k_0 is the wave number in vacuum. The parameter g determines the index profile. In general, the *NA* and g of the 50 µm GI-MMF are about 0.2 and 2, respectively. As a result, at 1550 nm, the number of modes that a 50 µm GI-MMF can support is in the hundreds. Due to the existence of multiple modes in the MMF and the interaction of the Brillouin-gain spectrum between each mode, the BGS broadens, and the sensing accuracy decreases [18,24,35]. Indeed, in the case of multiple modes, the BGS linewidth of the 50 µm GI-MMF obtained from our experiment is about 89.06 MHz, which is detrimental to improving the sensing accuracy. Moreover, the small effective refractive indexes of the higher-order modes in MMF make them less resistant to bending, which further affects the sensing reliability of the system [32].

In order to minimize the negative impact of the high-order modes in MMF on the sensing reliability, a short SMF is introduced into the graded-index multimode sensing fiber. An unconventional but simple and cheap distributed sensing structure is formed by aligning fusion to a short SMF near the end of the 50 µm GI-MMF. When the SMF alignment fuses to the 50 µm GI-MMF, only the axially symmetric optical modes in the MMF are excited. The coupling coefficient between the SMF and the fundamental mode in the MMF is above 90% [42]. Therefore, the optical mode content of the sensing structure is mainly the fundamental mode in the ideal case. However, in practice, due to the inherent inhomogeneity of the fiber and the influence of external disturbances, such as microbends and distortions, some optical modes will couple to become higher-order modes after a certain transmission distance. Nevertheless, the SMF at the start of the sensing structure filters out higher-order modes from the backscattering signal, which effectively reduces the interference caused by high-order modes. Therefore, the fused SMF acts as both a fundamental mode generator for the 50 µm GI-MMF and a high-order mode filter for the backscattering signal. Furthermore, the fundamental mode of the MMF has a stronger bending resistance, as the evanescent wave region of the fundamental mode in the MMF is much larger than that of the SMF [43], which is more conducive to the application of the sensing structure in the SSHM.

3. Experiment and Discussion

3.1. Measurement of Coupling Characteristics of SMF Alignment Fusion to 50 µm GI-MMF

In order to grasp the influence of SMF alignment fusion to the 50 µm GI-MMF on the sensing accuracy, we designed a simple system to measure and evaluate its power transmission characteristics. We draw on the fiber attenuation measurement method, an

insertion method, to evaluate the coupling efficiency between the two fibers. In theory, the cutback method is more accurate than the insertion method. However, in practice, the cut fiber still needs to be fused to a connector so that the light can be coupled into the optical power meter as much as possible so that the fusion quality has a direct impact on the measurement accuracy. Moreover, in order to reduce measurement errors, it is indispensable to measure the structures many times. However, the repeated cut-offs and fusions influence the measurement results significantly. The insertion method is relatively simple, repeatable, and can be used to reduce measurement errors by carrying out multiple measurements. Therefore, the insertion method was chosen to evaluate the coupling efficiency. The experimental setup to measure the coupling efficiency of the SMF alignment fusion to the GI-MMF is shown in Figure 3. The light source is a distributed feedback laser diode (LD). An isolator (ISO) is used to ensure the unidirectional transmission of light. A variable optical attenuator (VOA) is used to adjust the power in the fiber. The light from the LD enters the fiber through the optical circulator (OC), and the backward reflection light is separated into the other end port of the OC. As shown in Figure 3, we designed four structures, in which the black line represents SMF, and the green line represents the 50 μm GI-MMF. Four kinds of structures are formed by the alignment fusion between the optical fibers. It should be noted that the optical circulator can also be used to measure the backward reflection signal to characterize the coupling efficiencies of the sensing structures from another perspective. However, in our actual measurements, the backward reflection signals were weak and were not significantly different, with the exception of structure 4, which means that the measurement results are not accurate enough. Therefore, we did not carry out further comparative studies on the backward reflection signals that were measured.
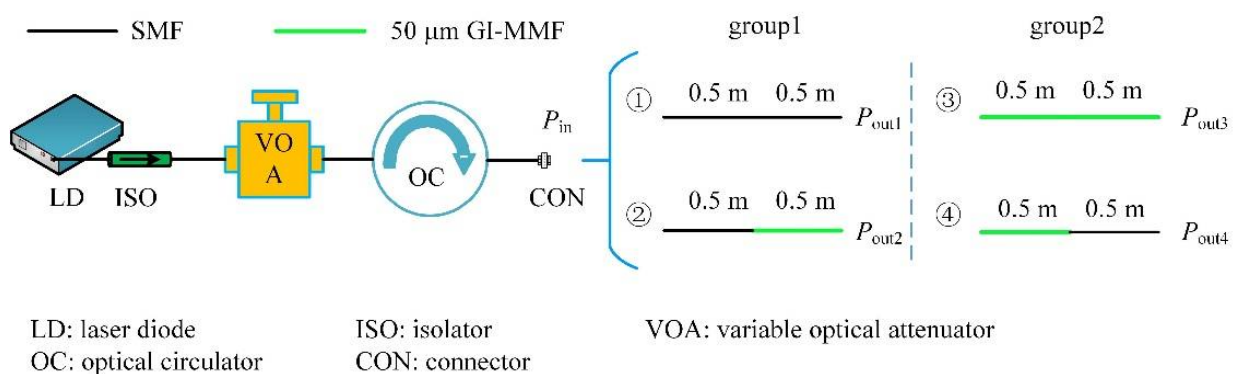

Figure 3. Experimental setup for measuring coupling efficiency.

After averaging the multiple measurement results, we obtained the relationship between the output optical power and the input optical power of the four structures, as shown in Figure 4. It is obvious that the output power of the four structures is essentially linearly correlated with the input power. Moreover, the output power of the first three structures is essentially the same as the input power, which indicates that almost no light is lost during the transmission process. The output power is slightly lower than the input power, which may be due to splicing loss. The output power of Structure 4 is quite different from the input power, which indicates that the light loss is relatively large in the transmission process. In order to evaluate the optical coupling efficiency of the bidirectional transmission between the SMF and 50 μm GI-MMF more accurately, we divided the four structures into two groups: the first group was used to assess the coupling efficiency from the SMF to the 50 μm GI-MMF, and the second group was used to assess the coupling efficiency from the 50 μm GI-MMF to the SMF. We treated the output optical power of Structure 1 as the input power of Structure 2, which is conducive to eliminating the influence of fiber-splicing loss. Similarly, the output power of Structure 3 is also regarded as the input power of Structure 4. The power difference is used to characterize the coupling efficiency of the SMF and 50 μm

GI-MMF, and the optical losses from the SMF to the 50 μm GI-MMF and from the 50 μm GI-MMF to the SMF are 0.106 dB and 1.35 dB, respectively. The difference in the optical coupling efficiency between the forward and backward modes in the sensing structure is caused by the effective area difference of the two fibers, which is also consistent with what most people assume.
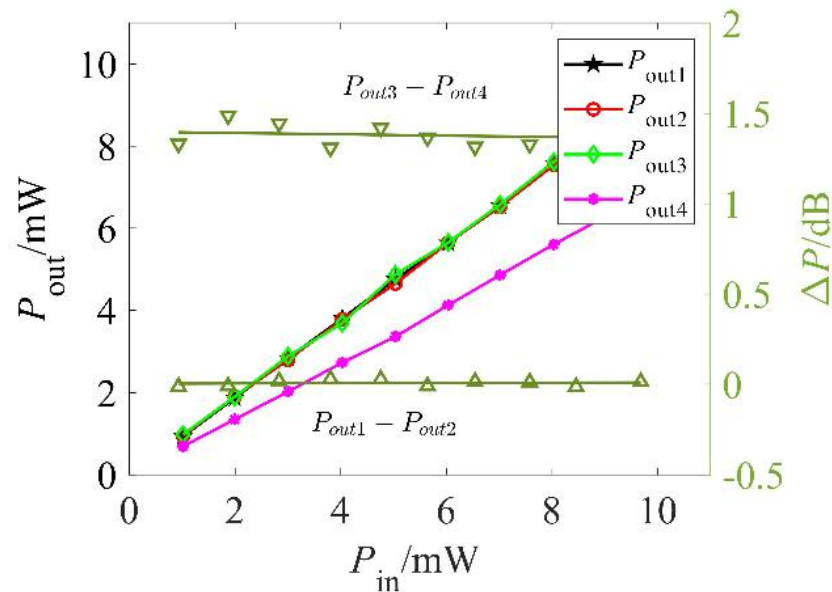

Figure 4. Optical power measurement results and comparison for four structures.

### 3.2. Experimental Verification of ISNR

Figure 5 shows a self-built frequency-shift local heterodyne BOTDR sensor, which was used to evaluate the ISNR of the sensing structure with the SMF alignment fusion to the 50 μm GI-MMF compared to the standard SMF. A polarization-maintaining coupler (PMC) with a splitting ratio of 50:50 splits the light from LD into two branches, a pump and a local oscillator (LO). An electro-optic modulator (EOM) driven by a pulse generator (PG) is used to modulate the amplitude of the light from the LD to generate a 130 ns pulse with a repetition rate of 16 kHz. The pulse light is amplified by an erbium-doped fiber amplifier (EDFA), which is filtered by a fiber Bragg grating (FBG) and adjusted by a VOA before being injected into the fiber under test (FUT) via a single-mode OC. A polarization scrambler (PS) is used to change the polarization state of the pump pulse to randomly reduce polarization fading noise (PFN). Taking the designed sensing structure as an example, the high-order modes in the scattering light generated by the multimode sensing fiber are first filtered out by the single-mode input fiber and then enter the EDFA for amplification. For the LO signal, the light from a lower branch is modulated by an EOM driven by a microwave generator (MG) to generate a carrier suppressed two sideband signals. After the two carrier-suppressed sidebands signals are amplified by an EDFA, and the amplified spontaneous emission noise (ASEN) and continuous anti-Stokes light are filtered out by a tunable optical filter (TOF). A PS was introduced to reduce the influence of the polarization noise on the heterodyne detection signal. A photoelectric detector (PD) is used to convert the heterodyned optical signal into an electrical signal and guide it to an electrical spectrum analyzer (ESA) for data superposition, averaging, acquisition, and processing.

From the above analysis, the pulse peak thresholds of the 50 μm GI-MMF and SMF are different, and the ratio is about 5. The pulse width in the experiment is 130 ns, corresponding to the spatial resolution of 13 m, which is limited by the ESA (N9020A-513), with a maximum resolution bandwidth of 8 MHz. For the SMF and 50 μm GI-MMF with a length of 5 km, the pulse-peak thresholds are about 2.67 W and 13.3 W, respectively. Given

that that the leakage light of the EOM will strengthen the SBS effect of the system, we set the pulse-peak power of the two sensing structures as 300 mW and 1.5 W, respectively. The BGS peak power of the two sensing structures was measured 20 times and averaged to obtain the Brillouin scattering signal trace at the central BFS, as shown in Figure 6. As seen from Figure 6, the designed sensing structure with an ISNR of 2.5 dB at the start and 1.3 dB at the end compared to the SMF yielded somewhat different values than the theoretical simulation values of 3.558 dB and 1.452 dB. On the one hand, this is due to the fact that the theoretical parameters do not exactly agree with the actual values. On the other hand, the high-order modes in the MMF are filtered out by the single-mode input fiber, resulting in the Brillouin scattering signal experiencing partial energy loss. Even so, the high-SNR characteristic of the proposed sensing structure has been proved effectively.
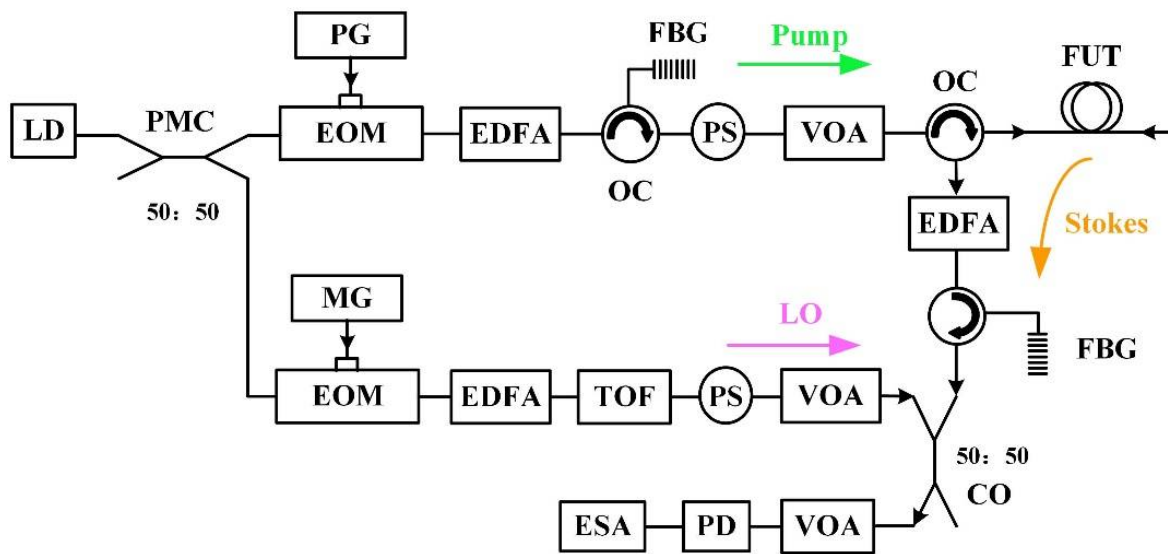

Figure 5. Experimental setup of BOTDR. PMC: polarization-maintaining coupler; PG: pulse generator; EOM: electro-optic modulator; EDFA: erbium-doped fiber amplifier; FBG: fiber Bragg grating; PS: polarization scrambler; MG: microwave generator; TOF: tunable optical filter; CO: coupler; PD: photoelectric detector; ESA: electrical spectrum analyzer.
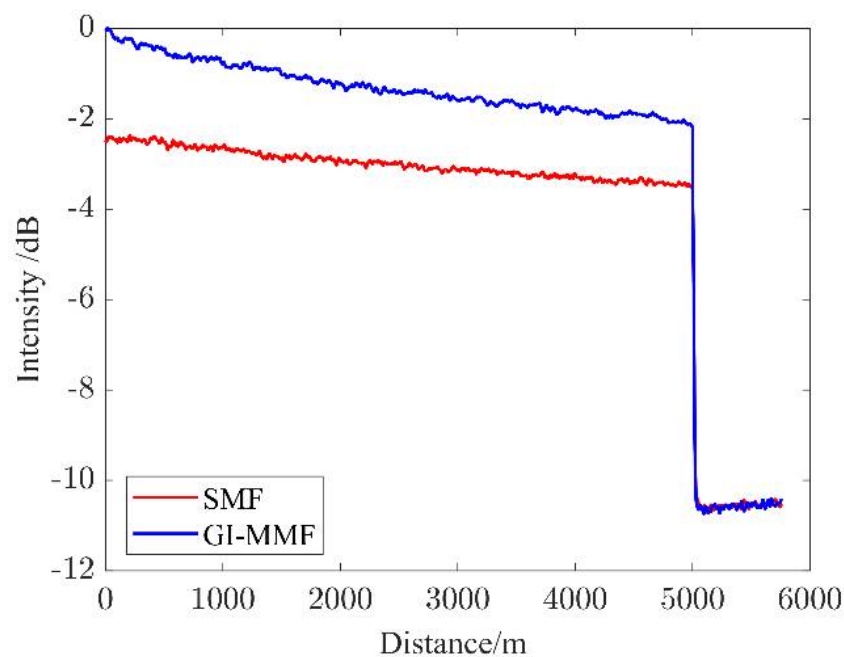
**Figure 6.** Trace of the measured Brillouin intensity.

3.3. Fresnel Reflection Elimination and Bending Characteristic Measurements

In general, the Fresnel reflection signal generated by the fiber end is not beneficial to the fiber-sensing system. The Fresnel reflection signal may damage the instruments on the one hand and affect the measurement accuracy on the other hand. In normal Brillouin-sensing experiments, knots that have been tied near the far end of the fiber can effectively eliminate the Fresnel-reflection signal. However, when the FUT was used as our sensing structure, we found that this approach was ineffective, which indicates that knots cannot effectively prevent the Fresnel reflection signal generated by the far end of fiber from returning to the beginning of the fiber. This interesting phenomenon indicates that the proposed sensing structure has a strong bending resistance. To eliminate the Fresnel reflection signal from the fiber end, we introduced 10 coils with different bending radii near the end of the sensing structure. We found that the Fresnel reflection signal of the sensing structure was mostly eliminated when the diameter of the fiber coil was 2.5 mm, which is impossible in practical applications. Therefore, we fused a short 50 μm GI-MMF with an angled polished connector (APC) to the end of the sensing structure, and the Fresnel reflection signal was almost completely eliminated; however, when a fiber dust cap was covering the APC end, a strong Fresnel reflection signal was observed again. The experimental results are shown in Figure 7.
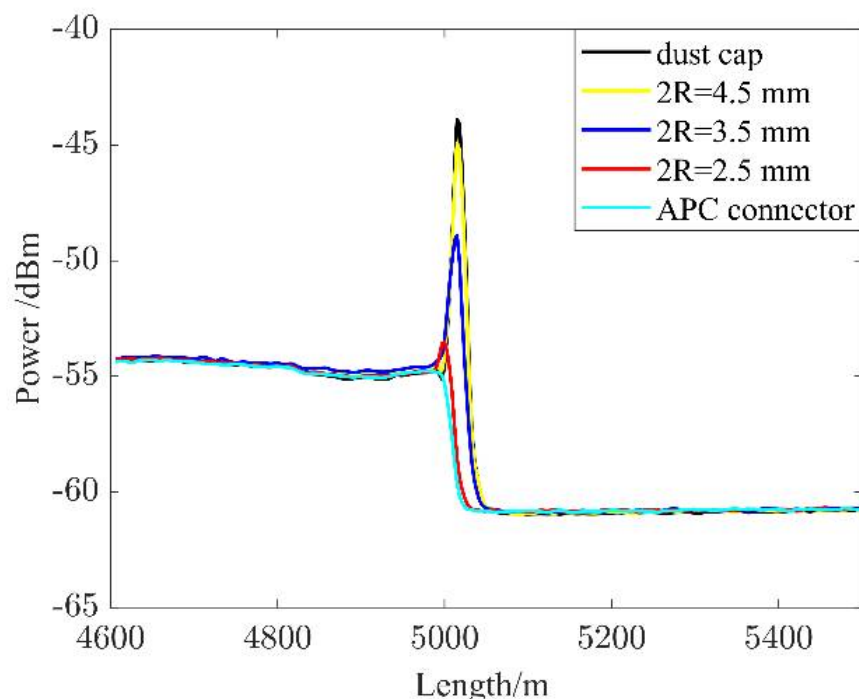
Figure 7. Measured Fresnel reflection signal with different coil radii.

To further evaluate the bending resistance, we performed bending tests on the SMF and the proposed sensing structure with the system shown in Figure 5. The experiments were carried out by winding a length of fiber into 10 coils with different bending radii at the same position along approximately 4.8 km of the 5 km FUTs. The signal loss was visually displayed by the Brillouin intensity along the entire fiber. The Brillouin signals of the FUTs at different bending radii were measured several times, and the averaged Brillouin signal distribution is shown in Figure 8. It can be clearly seen that the SMF shows no obvious signal loss at the bending radius of 16 mm, and the proposed sensing structure is 2.25 mm. Obviously, the sensing structure of the SMF alignment fusion to the 50 μm GI-MMF has a far better bending resistance than the SMF, which makes it more suitable for SSHM applications.
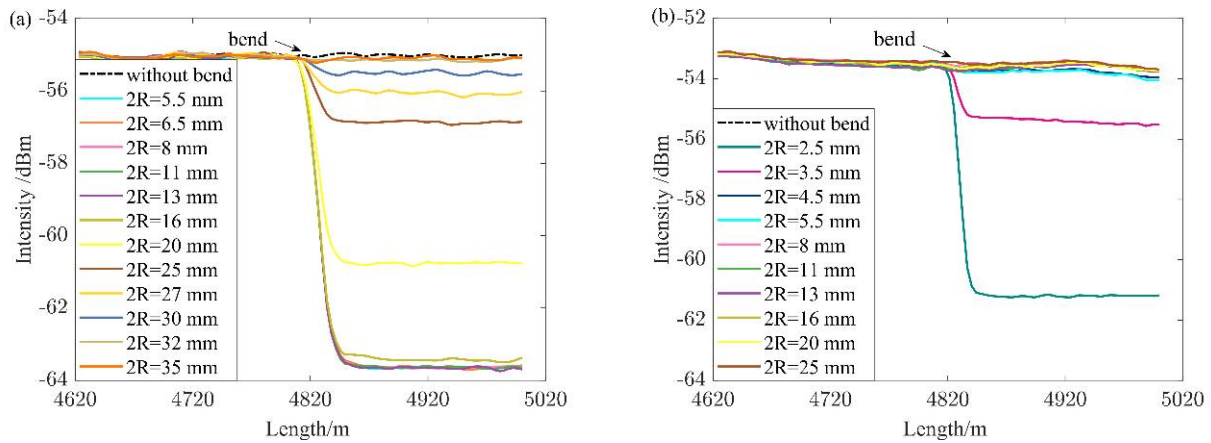
Figure 8. Measured Brillouin signals intensity with different bending radii. (**a**) SMF; (**b**) SMF alignment fusion to 50 μm GI-MMF.

3.4. Temperature-Sensing Characteristics

From the previous analysis and experimental verification, it can be seen that the proposed sensing structure has a strong SNR and bending resistance. Therefore, using the experimental system shown in Figure 5, we measured the temperature-sensing characteristics of SMF alignment fusion to the 50 μm GI-MMF. At room temperature (24 °C), an approximated 150 m fiber near the far end of the 50 μm GI-MMF was heated from 35 °C to 75 °C at a step of 10 °C. Three measurements were carried out at the same temperature, and the measured results were averaged by extracting the parameters of the Brillouin signal more accurately.

The measurement results are shown in Figure 9. Figure 9a shows a three-dimensional BGS of the 5 km sensing structure when the heating section was set to 75 °C. Figure 9b shows the BFS of the sensing structure at different temperatures. Figure 9c shows an excellent linear relationship between the BFS and temperature. The BFS variation sensitivity to temperature is 0.946 MHz/°C, which is basically consistent with the conventional SMF. The BGS at 4.85 km of the sensing structure at different temperatures is shown in Figure 9d. It can be seen that the BFS of the sensing structure increases significantly as the temperature increases. The maximum BFS fluctuation in the heating section is 0.928 MHz, and thus, a temperature error of 1 °C can be obtained with the calibration temperature coefficient. These experimental results demonstrate that the sensing structure of the SMF alignment fusion to the 50 μm GI-MMF has a good sensing performance in the BOTDR system.

It should be noted that the BGS linewidth of the proposed sensing structure is about 53.2 MHz due to the existence of the single-mode input fiber, which is significantly superior to the entire MMF sensing structure. The BGS linewidth affects the BFS accuracy, which, in turn, affects the sensing reliability. The BFS accuracy can be expressed as [44]

$$\delta v_{\mathrm{B}} = \frac{\Delta v_{\mathrm{B}}}{\sqrt{2}\left(R_{\mathrm{SN}}\right)^{1/4}} \tag{18}$$

where R_{SN} is the system SNR, and Δv_{B} is the spontaneous BGS linewidth.

At room temperature, the average SNRs at the 300 m end of the SMF and the proposed sensing structure are 25.6 dB and 27.1 dB, respectively, and the average BGS linewidths are about 32.5 MHz and 53.2 MHz, respectively. Therefore, the BFS accuracies of the SMF and the proposed sensing structure are 5.265 MHz and 7.905 MHz, respectively. It can be seen that, although the proposed sensing structure can obtain a higher SNR, the accuracy of the BFS is lower than that of the SMF due to the larger BGS linewidth.

In order to weigh the influence of the SNR and BGS linewidths on the BFS accuracy of the SMF and the proposed sensing structure more intuitively, we calculated the SNR

relationship between the two sensing structures under the condition of consistent BFS accuracy. This equation can be expressed as follows:

$$\frac{\Delta v_{\text{BS}}}{\sqrt{2}(R_{\text{SNS}})^{\frac{1}{4}}} = \frac{\Delta v'_{\text{B}}}{\sqrt{2}\left(R'_{\text{SN}}\right)^{\frac{1}{4}}} \tag{19}$$

where Δv_{BS} and $\Delta v'_{\text{B}}$, R_{SNS} and R'_{SN} are the BGS linewidth and SNR of the SMF and proposed sensing structure, respectively. Therefore, the SNR relationship can be expressed as

$$R_{\text{SNS}}(\text{dB}) = R'_{\text{SN}}(\text{dB}) - 8.6(\text{dB}) \tag{20}$$
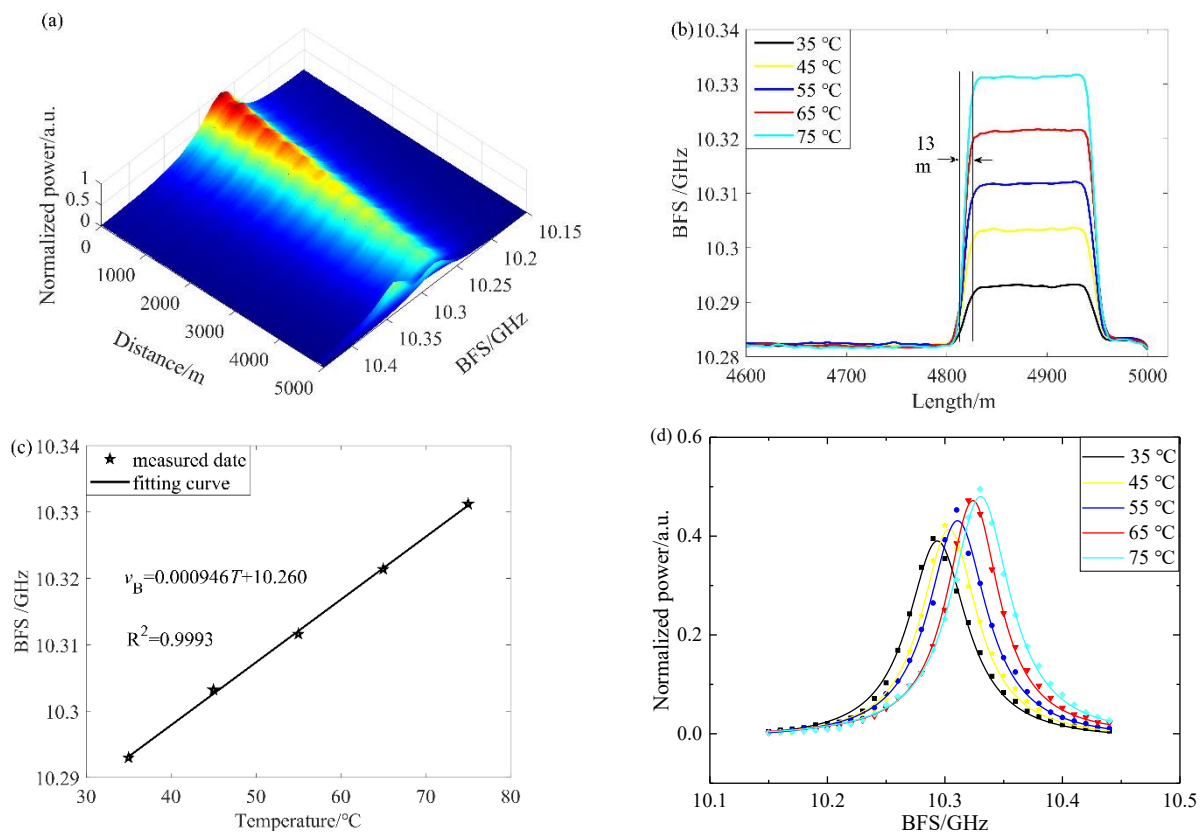
Figure 9. Temperature measurement results of SMF alignment fusion to 50 μm GI-MMF. (**a**) three-dimensional BGS of the whole sensing structure at a heating section of 75 °C; (**b**) BFS at 35–75 °C; (**c**) Linear fitting between BFS and temperature; (**d**) BGS at different temperatures.

It can be seen that when the SNR of the proposed sensing structure is 8.6 dB higher than that of the SMF, the BFS accuracy of the two sensing structures are consistent. Therefore, we may be able to combine the proposed sensing structure with pulse coding technology or multi-wavelength technology to further improve the SNR and achieve a BFS accuracy that is equivalent to that of the SMF. In other words, the high-SNR characteristic and outstanding bending resistance of the sensing structure come at the expense of the BFS accuracy. Taking the combination of other techniques, such as pulse coding or multi-wavelength technology, into account to further improve the SNR system as well as its usability and cost performance in practical engineering applications, we believe that the proposed sensing structure implementing SMF alignment fusion to a 50 μm GI-MMF has great potential in the SSHM infrastructure.

4. Conclusions

In conclusion, we reported and experimentally validated SMF alignment fusion to a 50 μm GI-MMF as a simple and low-cost sensing structure that can be implemented in BOTDR. The theoretical analysis and detailed experimental studies carried out in this work show that the proposed sensing structure has a higher SNR and bending resistance than the SMF and that it has a smaller BGS linewidth than the entire MMF structure. The experimentally measured ISNR of the sensing structure over the SMF at the beginning and end of a 5 km fiber are 2.5 dB and 1.3 dB, respectively. The minimum bending radius of the sensing structure is 2.25 mm, which is much better than that of the SMF. Moreover, we designed a simple system to evaluate the bidirectional optical coupling efficiency of the SMF and 50 μm GI-MMF. Losses from the SMF to the 50 μm GI-MMF and from the 50 μm GI-MMF to the SMF are different due to different effective areas of the fibers, which are 0.106 dB and 1.35 dB, respectively. Finally, we measured the temperature-sensing characteristics of the designed sensing structure, using the self-built frequency-shifted local heterodyne BOTDR system, and we obtained a temperature sensitivity of 0.946 MHz/°C and a measurement accuracy of 1 °C, which indicates its reliability in the SSHM infrastructure.

References

1. Hu, D.J.J.; Humbert, G.; Dong, H.; Zhang, H.; Hao, J.; Sun, Q. Review of specialty fiber based Brillouin optical time domain analysis technology. *Photonics* **2021**, *8*, 421. [CrossRef]
2. Hu, T.; Hou, G.; Li, Z. The field monitoring experiment of the roof strata movement in coal mining based on DFOS. *Sensors* **2020**, *20*, 1318. [CrossRef] [PubMed]
3. Gu, K.; Shi, B.; Liu, C.; Jiang, H.; Li, T.; Wu, J. Investigation of land subsidence with the combination of distributed fiber optic sensing techniques and microstructure analysis of soils. *Eng. Geol.* **2018**, *240*, 34–47. [CrossRef]
4. Feng, T.; Zhou, J.; Shang, Y.; Chen, X.; Yao, X. Distributed transverse-force sensing along a single-mode fiber using polarization-analyzing OFDR. *Opi. Express* **2020**, *28*, 31253–31271. [CrossRef]
5. Zhang, X. *Distributed Optical Fiber Sensing Techniques*; Science Press: Beijing, China, 2013; pp. 1–25.
6. Liu, T.; Liu, K.; Dai, L.; Jiang, J.; Wang, J.; Ding, Z.; Sang, M.; Hu, H.; Wang, S.; Xue, C.; et al. Research progress of key technologies in recognition sensing for opto-electronic information and event. *Acta Optica Sin.* **2021**, *41*, 0106002. [CrossRef]
7. Dong, Y. High-performance distributed Brillouin optical fiber sensing. *Photonic Sens.* **2021**, *11*, 69–90. [CrossRef]
8. Bi, W.; Yang, X.; Li, J.; Fu, X.; Fu, G. Forward and backward Raman amplification of Brillouin scattering signal in Brillouin optical time domain reflectometer system. *Chin. J. Lasers* **2014**, *41*, 1205007. [CrossRef]
9. Mizuno, Y.; Theodosiou, A.; Kalli, K.; Liehr, S.; Lee, H.; Nakamura, K. Distributed polymer optical fiber sensors: A review and outlook. *Photonics Res.* **2021**, *9*, 1719–1733. [CrossRef]
10. Maughan, S.M.; Kee, H.H.; Newson, T.P. Simultaneous distributed fibre temperature and strain sensor using microwave coherent detection of spontaneous Brillouin backscatter. *Meas. Sci. Technol.* **2001**, *12*, 834–842. [CrossRef]
11. Shimizu, K.; Horiguchi, T.; Koyamada, Y.; Kurashima, T. Coherent self-heterodyne detection of spontaneously Brillouin-scattered light waves in a single-mode fiber. *Opt. Lett.* **1993**, *18*, 185–187. [CrossRef]

12. Minakawa, K.; Mizuno, Y.; Nakamura, K. Cross effect of strain and temperature on Brillouin frequency shift in polymer optical fibers. *J. Lightwave Technol.* **2017**, *35*, 2481–2486. [CrossRef]
13. Lee, C.C.; Chiang, P.W.; Chi, S. Utilization of a dispersion-shifted fiber for simultaneous measurement of distributed strain and temperature through Brillouin frequency shift. *IEEE Photonics Technol. Lett.* **2001**, *13*, 1094–1096. [CrossRef]
14. Li, A.; Wang, Y.; Fang, J.; Li, M.; Kim, B.Y.; Shieh, W. Few-mode fiber multi-parameter sensor with distributed temperature and strain discrimination. *Opt. Lett.* **2015**, *40*, 1488–1491. [CrossRef] [PubMed]
15. Song, K.Y.; Kim, Y.H. Characterization of stimulated Brillouin scattering in a few-mode fiber. *Opt. Lett.* **2013**, *38*, 4841–4844. [CrossRef]
16. Zou, W.; He, Z.; Kishi, M.; Hotate, K. Stimulated Brillouin scattering and its dependences on strain and temperature in a high-delta optical fiber with F-doped depressed inner cladding. *Opt. Lett.* **2007**, *32*, 600–602. [CrossRef]
17. Zou, L.; Bao, X.; Afshar, V.S.; Chen, L. Dependence of the Brillouin frequency shift on strain and temperature in a photonic crystal fiber. *Opt. Lett.* **2004**, *29*, 1485–1487. [CrossRef]
18. Tommya, B.; Guillaumea, B.; Steevea, M.; Younsa, M.; Richardb, F.; Françoisc, T.; Martinaet, B. Curvature sensing using a hybrid polycarbonate-silica multicore fiber. *Opt. Express* **2020**, *28*, 39387–39399. [CrossRef]
19. Mohamed, A.S.Z.; Wang, M.; Giovanni, M.; Li, M.; Li, S.; Huang, Y.; Wang, T.; Chen, K.P. Discrimination of temperature and strain in Brillouin optical time domain analysis using a multicore optical fiber. *Sensors* **2018**, *18*, 1176. [CrossRef]
20. Kuyt, G. Fast progress in ITU for bend-loss insensitive singlemode fiber. *Lightwave* **2007**, *24*, 19.
21. Zhang, Z.; Lu, Y.; Pan, Y.; Bao, X.; Chen, L. Trench-assisted multimode fiber used in Brillouin optical time domain sensors. *Opt. Express* **2019**, *27*, 11396–11405. [CrossRef]
22. Ren, G.; Lin, Z.; Zheng, S.; Jian, S. Resonant coupling in trenched bend-insensitive optical fiber. *Opt. Lett.* **2013**, *38*, 781–783. [CrossRef] [PubMed]
23. Watekar, P.R.; Ju, S.; Yoon, Y.S.; Lee, Y.S.; Han, W.T. Design of a trenched bend insensitive single mode optical fiber using spot size definitions. *Opt. Express* **2008**, *16*, 13545–13551. [CrossRef] [PubMed]
24. Nakajima, K.; Hogari, K.; Jian, Z.; Tajima, K.; Sankawa, L. Hole-assisted fiber design for small bending and splice losses. *IEEE Photonics Technol. Lett.* **2003**, *15*, 1737–1739. [CrossRef]
25. Saitoh, K.; Tsuchida, Y.; Koshiba, M. Bending-insensitive single-mode hole-assisted fibers with reduced splice loss. *Opt. Lett.* **2005**, *30*, 1779–1781. [CrossRef]
26. Tsuchida, Y.; Saitoh, K.; Koshiba, M. Design and characterization of single-mode holey fibers with low bending losses. *Opt. Express* **2005**, *13*, 4770–4779. [CrossRef]
27. Wang, Z.; Zhao, C.; Jin, S. Design of a bending-insensitive single-mode photonic crystal fiber. *Opt. Fiber Technol.* **2013**, *19*, 213–218. [CrossRef]
28. Behera, B.L.; Maity, A.; Varshney, S.K.; Datta, R. Theoretical investigations of trench-assisted large mode-area, low bend loss and single-mode microstructured core fibers. *Opt. Commun.* **2013**, *307*, 9–16. [CrossRef]
29. Martelli, C.; Canning, J.; Gibson, B.; Huntington, S. Bend loss in structured optical fibres. *Opt. Express* **2007**, *15*, 17639–17644. [CrossRef]
30. Zailani, N.F.H.; Saidin, N.; Rusdi, M.F.M.; Harun, S.W.; Thirunavakkarasu, P.M. Acetone liquid sensing based on fiber optic Mach-Zehnder interferometer. In Proceedings of the 2021 IEEE Regional Symposium on Micro and Nanoelectronics (RSM), Kuala Lumpur, Malaysia, 2–4 August 2021. [CrossRef]
31. Akbarpour, Z.; Ahmadi, V.; Roghabadi, F.A. Refractive index sensor based on wavelength shift analysis in MSM optical fiber structure. In Proceedings of the 28th Iranian Conference on Electrical Engineering (ICEE), Tabriz, Iran, 4–6 August 2020. [CrossRef]
32. Li, Y.; Fan, H.; Zhang, L.; Wang, K.; Wu, G.; Liu, Z. A bend-resistant BOTDR distributed fiber sensor. *Opt. Commun.* **2022**, *514*, 128110. [CrossRef]
33. Sodhi, S.S.; Jackman, W.S. Strain measurement in multimode fibers using Brillouin optical time-domain reflectometry. In Proceedings of the Optical Fiber Communication Conference, San Jose, CA, USA, 22–27 February 1998. [CrossRef]
34. Minardo, A.; Bernini, R.; Zeni, L. Analysis of the Brillouin gain spectrum in a graded-index multimode fiber. In Proceedings of the Third Mediterranean Photonics Conference, Trani, Italy, 7–9 May 2014. [CrossRef]
35. Mocofanescu, A.; Wang, L.; Jain, R.; Shaw, K.D.; Gavrielides, A.; Peterson, P.; Sharma, M.P. SBS threshold for single mode and multimode GRIN fibers in an all fiber configuration. *Opt. Express* **2005**, *13*, 2019–2024. [CrossRef]
36. Iezzi, V.L.; Loranger, S.; Harhira, A.; Rehman, S. Stimulated Brillouin scattering in multi-mode fiber for sensing applications. In Proceedings of the 7th International Workshop on Fiber and Optical Passive Components, Montreal, QC, Canada, 13–15 July 2011. [CrossRef]
37. Li, Y.; Zhao, X.; Zhao, L.; Ma, L.; Li, X.; An, Q. Brillouin scattering parameters of different modes in multimode optical fibers. *Acta Photonica Sin.* **2015**, *44*, 27–33. [CrossRef]
38. Bayvel, P.; Radmore, P.M. Solutions of the SBS equations in single mode optical fibers and implications for fiber transmission systems. *Electron. Lett.* **1990**, *26*, 434–436. [CrossRef]
39. Li, C.; Lu, Y.; Zhang, X.; Wang, F. SNR enhancement in Brillouin optical time domain reflectometry using multi-wavelength coherent detection. *Electron. Lett.* **2012**, *48*, 1–3. [CrossRef]
40. Horiguchi, T.; Tateda, M. BOTDA-nondestructive measurement of single-mode optical fiber attenuation characteristics using Brillouin interaction: Theory. *J. Lightwave Technol.* **1989**, *7*, 1170–1176. [CrossRef]

41. Gu, W.; Huang, Y.; Chen, X.; Zhang, J.; Zhang, M.; Yu, S. *Optical Fiber Communication*; Posts & Telecommunications Press: Beijing, China, 2011; pp. 1–26.

42. Minardo, A.; Bernini, R.; Zeni, L. Experimental and numerical study on stimulated Brillouin scattering in a graded-index multimode fiber. *Opt. Express* **2014**, *22*, 17480–17489. [CrossRef]

43. Donlagić, D.; Brianb, C. Propagation of the fundamental mode in curved graded index multimode fiber and its application in sensor systems. *J. Lightwave Technol.* **2000**, *18*, 334–342. [CrossRef]

44. Cui, Q.; Pamukcu, S.; Lin, A.; Xiao, W.; Toulouse, J. Performance of double sideband modulated probe wave in BOTDA distributed fiber sensor. *Microwave Opt. Technol. Lett.* **2010**, *52*, 2713–2717. [CrossRef]